ACS APPLIED MATERIALS & INTERFACES

Research Article

www.acsami.org

Synthesis and Modeling of Uniform Complex Metal Oxides by Close-Proximity Atmospheric Pressure Chemical Vapor Deposition

Robert L. Z. Hoye,[†] David Muñoz-Rojas,[†,‡] Kevin P. Musselman,[§,†] Yana Vaynzof,[§,∥] and Judith L. MacManus-Driscoll*,[†]

[†]Department of Materials Science and Metallurgy, University of Cambridge, 27 Charles Babbage Road, Cambridge CB3 0FS, U.K.

[‡]LMGP, University Grenoble-Alpes, CNRS, F-38000 Grenoble, France

[§]Department of Physics, University of Cambridge, JJ Thomson Avenue, Cambridge CB3 0HE, U.K.

Supporting Information

ABSTRACT: A close-proximity atmospheric pressure chemical vapor deposition (AP-CVD) reactor is developed for synthesizing high quality multicomponent metal oxides for electronics. This combines the advantages of a mechanically controllable substrate-manifold spacing and vertical gas flows. As a result, our AP-CVD reactor can rapidly grow uniform crystalline films on a variety of substrate types at low temperatures without requiring plasma enhancements or low pressures. To demonstrate this, we take the zinc magnesium oxide ($Zn_{1-x}Mg_xO$) system as an example. By introducing the precursor gases vertically and uniformly to the substrate across the gas manifold, we show that films can be produced with only 3% variation in thickness over a 375 mm^2 deposition area. These thicknesses are significantly more uniform than for films from previous AP-CVD reactors. Our films are also compact, pinhole-free, and have a thickness that is linearly controllable by the number of oscillations of the substrate beneath the gas manifold. Using photoluminescence and X-ray diffraction measurements, we show that for Mg contents below 46 at. %, single phase $Zn_{1-x}Mg_xO$ was produced. To further optimize the growth conditions, we developed a model relating the composition of a ternary oxide with the bubbling rates through the metal precursors. We fitted this model to the X-ray photoelectron spectroscopy measured compositions with an error of $\Delta x = 0.0005$. This model showed that the incorporation of Mg into ZnO can be maximized by using the maximum bubbling rate through the Mg precursor for each bubbling rate ratio. When applied to poly(3-hexylthiophene-2,5-diyl) hybrid solar cells, our films yielded an open-circuit voltage increase of over 100% by controlling the Mg content. Such films were deposited in short times (under 2 min over 4 cm^2).

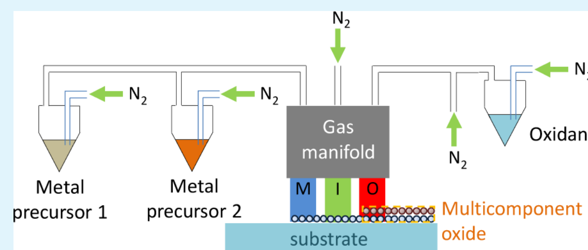

KEYWORDS: *atmospheric pressure chemical vapor deposition, zinc magnesium oxide, multicomponent metal oxides, bandgap tuning, solar cells, spatial atmospheric atomic layer deposition*

INTRODUCTION

Metal oxides are widely used for optoelectronic applications,[1−3] due to their stability, composition of nontoxic and earth-abundant elements, and intrinsic semiconductivity.[4] It is crucial that these metal oxides can be produced scalably, so that the devices can be manufactured on an industrial level.[4] Chemical vapor deposition (CVD) is an appealing metal oxide deposition technique, due to the high growth rates possible,[5,6] but CVD is limited by requiring high deposition temperatures (often >350 °C),[7] with plasmas or low pressure processing needed to reduce deposition temperatures.[6−8] Atomic layer deposition (ALD) is another appealing metal oxide deposition technique. ALD is a subset of CVD[6] but only involves surface half-reactions,[9] rather than the gas-phase and surface reactions used in CVD.[6] This allows uniform films with nanometer-level thickness control to be deposited at lower temperatures (∼120 °C for ZnO) conformally onto both flat substrates and high aspect-ratio substrates.[9−11] Growing films below 155 °C is important for compatibility with flexible polymer substrates, in addition to a lower energy consumption.[12,13] ALD is, however, limited by lower growth rates because it separates the exposure of the metal precursors and oxidant to the substrate in time by purging a closed-reaction chamber between each pulse.[12,13] Atmospheric pressure spatial atomic layer deposition (AP-SALD) overcomes these limitations by spatially separating the precursors.[13,14] AP-SALD is commonly implemented with the close-proximity design,[13,15−17] in which the substrate is oscillated <100 μm beneath a manifold containing spatially separated parallel gas channels, as illustrated in refs 14 and 18. By moving the substrate beneath these gas channels, the metal precursor and oxidant separately chemisorb onto the substrate to grow the metal oxide monolayer by monolayer up to 2 orders of magnitude faster than conventional ALD.[12,16] In some AP-SALD reactors, such as that designed by Levy et al.,[18] the

Received: October 23, 2014
Accepted: May 5, 2015
Published: May 5, 2015

ACS Publications © 2015 American Chemical Society

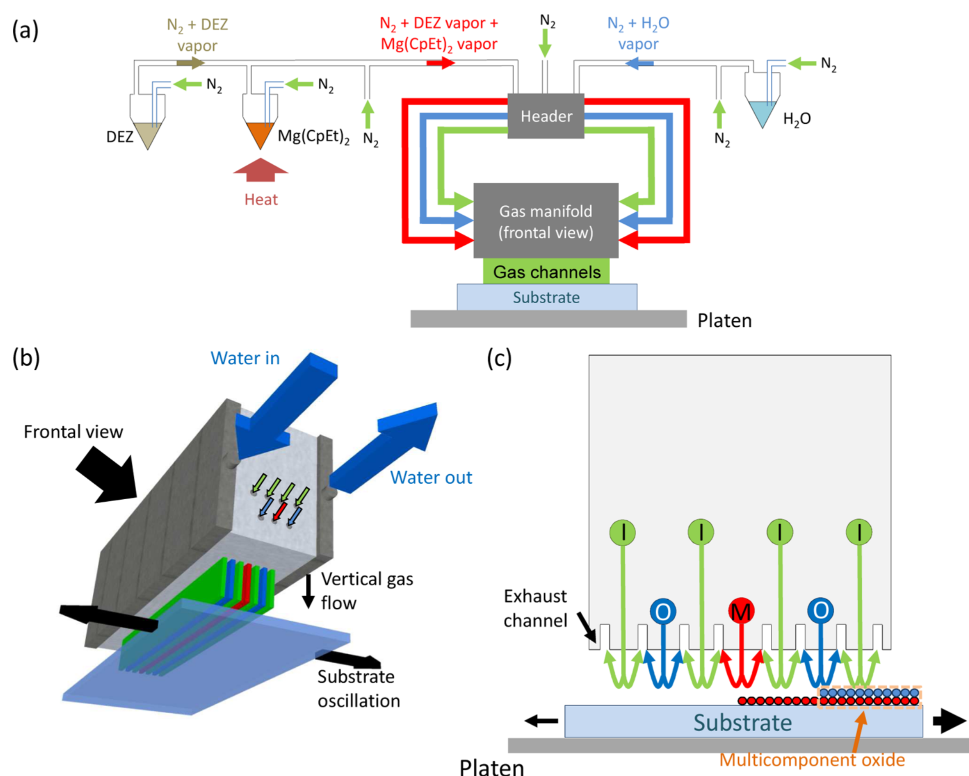

Figure 1. Illustration of our AP-CVD reactor. (a) Schematic showing that inert nitrogen gas is bubbled through the precursors and introduced to the gas manifold via a header. (b) Three dimensional view of the gas manifold showing how gases from the header are introduced to the side of the manifold (gas channels on the other side are hidden from view) and guided to flow vertically down to the oscillating substrate. The blue arrows indicate the water circulated in and out of the metal plates encasing the reactor to maintain it at a constant temperature during operation. The platen is not shown for clarity. (c) Schematic of the side of the gas manifold showing the gas flow. "M" represents the metal precursor, "I" the inert gas, and "O" the oxidant gas channels. The substrate is loaded onto a platen (metal plate with vacuum holes to hold the substrate in place), which heats the sample and oscillates beneath the gas manifold.

gas manifold is mechanically constrained over the substrate, meaning that a large manifold−substrate spacing can occur.[14,17,18] This can lead to intermixing between the gas channels and the film depositing by CVD,[19] meaning that the reactor can operate in both AP-SALD mode and AP-CVD mode.[14] Operating in AP-CVD mode has the advantage of higher growth rates.[14] This is highly desirable for depositing onto flat, featureless substrates (i.e., not requiring the high conformality of conventional ALD) on an industrial scale. An example is producing metal oxides thin films for solar cells.[17]

A significant limitation of some close-proximity reactors operating in AP-CVD mode is a lack of film uniformity. For example, the reactor detailed in refs 17 and 18 introduces precursor gases from one side of the gas manifold before flowing across to the exhaust on the other side. This results in films being thicker close to the inlet. Nonuniform films also occur in other AP-CVD reactors due to asymmetric gas flows.[20] A thickness-variation is highly undesirable when thickness-related effects strongly influence electronic device performance[21] or when thickness-sensitive measurements need to be performed, such as Hall-effect measurements. Film uniformity has been addressed in more recent AP-SALD designs by introducing the precursor gases vertically to the substrate.[12,14,19,22] However, these reactors use gas bearings to float the manifold over the substrate[12,23,24] or the substrate over the manifold.[19,25] While the use of gas bearings is advantageous for large-area rigid and polymer substrates,[22] mechanically constraining the manifold over the substrate, as occurs in the design by Levy et al.,[18] is advantageous by providing flexibility in the type of substrate onto which the film is deposited. These include large glass plates, small ITO/glass substrates, or curved and fragile thermally oxidized Cu_2O.[26] Vertical gas flows have also appeared in a recent AP-CVD reactor design,[23] but as with most other CVD reactors, the deposition temperature needed to be over 380 °C because the film synthesis was dependent on gas-phase reactions rather than only surface reactions.[23] Overcoming these uniformity and growth temperature limitations in AP-CVD reactors is important for the electronics industry that is becoming increasingly reliant on high-quality, uniform semiconducting oxides for devices.[27−29] It is also essential that the reactor has a high growth rate, allows fine control over the film properties, and that the films are compact with good functionality.[15,17] The precursor vapor pressure, reactivity, and saturation in the gas stream are important as well, especially for multicomponent oxides. Incorporating new elements into binary oxides to tune their electronic properties (such as bandgap[30,31] and carrier concentration[3,32,33]) has been extensively shown to be important for maximizing device performance,[3,4,30−33] but a pressing challenge is that these precursor properties are difficult to directly measure and often unknown for new or rarely used organometallic precursors.

In this work, we detail an AP-CVD gas manifold design enabling uniform multicomponent metal oxide films to be grown at high rates at temperatures not exceeding 150 °C. This design combines the uniformity achievable through vertical gas flows with the ability to control the substrate-manifold spacing independently of the gas flow rates. We demonstrate the significant advantages of this design with zinc magnesium oxide

DOI: 10.1021/am5073589
ACS Appl. Mater. Interfaces 2015, 7, 10684−10694

($Zn_{1-x}Mg_xO$) as an example material. While we have used our reactor to produce the $Zn_{1-x}Mg_xO$ used in some of our previous works,[21,26,34,35] we have never reported on the design principles enabling its capability of producing uniform, crystalline films rapidly at low temperatures. The quality of doping using this reactor is characterized through photoluminescence and X-ray diffraction measurements. By developing and fitting a model, we determine how to improve the growth conditions for incorporating Mg into ZnO without having to measure the incorporation rates and saturation of each precursor. The design we present can be implemented by researchers requiring uniform, rapidly synthesized, high-quality oxides for electronics on both laboratory and industrial scales.

EXPERIMENTAL SECTION

Deposition of Zinc Magnesium Oxide Thin Films. Our reactor is adapted from that first reported by Levy et al.[18] One important beneficial feature of our gas manifold design is that instead of guiding the gas flow horizontally across the bottom of the manifold, the gases are flowed vertically downward to the substrate. This flow is uniform across the manifold. As illustrated in Figure 1, the precursor and inert gases are introduced from both sides of the manifold to gas channels that run through its length. The manifold is designed so that a uniform pressure profile is established across it. The channels running down to the substrate within the gas manifold (Figure 1c) ensure gas flow vertically to the substrate. Moving the substrate repeatedly through the different gas channels (alternation of metal precursor, inert gas and oxidant) beneath the gas manifold allows each precursor to be exposed to the substrate. This enables uniform film growth with each cycle. The gas manifold is mechanically constrained over the substrate, which allows the substrate-manifold spacing to be controlled. This, in part, allows the reactor to operate in AP-CVD mode. It also allows the spacing to accommodate for the size of the substrate. A variety of substrates, whether 25 cm^2 glass, 14 mm × 14 mm ITO/glass, plastic, thermally oxidized Cu_2O,[26] or temperature-sensitive organometal halide perovskites[34] can thus be loaded onto a platen that heats the substrate and oscillates it beneath the manifold (Figures 1a,c). These substrates can be unloaded from the platen immediately once the deposition has been completed.

Zinc magnesium oxide ($Zn_{1-x}Mg_xO$) films were deposited onto indium tin oxide substrates (ITO; Praezisions Glas & Optik) using our reactor. These substrates were 14 mm × 14 mm × 0.7 mm and had 180 nm of ITO (sheet resistance <10 Ω/sq). We also deposited onto 0.7 mm thick borosilicate glass, which was cut to 14 mm × 14 mm squares for film characterization. Films deposited on the ITO were also used for characterization and device fabrication. The glass and ITO substrates were ultrasonically cleaned in isopropanol for 15 min and blown dry with compressed air. The substrates were fitted within a 0.7 mm thick mask on the platen. This mask had a 14 mm by 28 mm rectangular hole to fit two substrates and to ensure that the deposition area was flat to maximize the homogeneity of the gas flows and thickness of the deposited film. The platen was heated to 150 °C and oscillated at 50 mm·s^{-1} 50 μm beneath the gas manifold (maintained at 40 °C). Diethylzinc (DEZ, from Sigma-Aldrich) was used as the Zn precursor and bis(ethylcyclopentadienyl)magnesium) ($Mg(CpEt)_2$, from Strem Chemicals Inc.) as the magnesium precursor. Caution needs to be taken when handling DEZ and $Mg(CpEt)_2$ since these are pyrophoric and should never come into contact with air or moisture. To deposit intrinsic ZnO, nitrogen gas (<10 ppb oxygen and <20 ppb H_2O) was bubbled through DEZ at 25 mL·min^{-1}, and this was diluted with 100 mL·min^{-1} nitrogen gas in the metal precursor line, which was fed to the gas manifold. This rapidly flows to the gas manifold (section S1, Supporting Information). Nitrogen gas was also bubbled through water at 100 mL·min^{-1} as the oxidant, and this was diluted with 200 mL·min^{-1} nitrogen gas before being fed to the gas manifold. Nitrogen gas flowing at 500 mL·min^{-1} was also directly fed to the gas manifold to supply the nitrogen gas for the inert gas channels. For zinc magnesium oxide, the only difference in the gas flows was that nitrogen gas was bubbled through DEZ and $Mg(CpEt)_2$ at different rates. The $Mg(CpEt)_2$ was also heated to 55 °C under optimum conditions. DEZ was maintained at room temperature. Our method for optimizing the deposition of $Zn_{1-x}Mg_xO$ by controlling this gas mixture is detailed in section S2 of the Supporting Information and the final flow conditions used given in Table 1.

Table 1. Absolute Bubbling Rates and Growth Rates for Each Bubbling Rate Ratio[a]

F[$Mg(CpEt)_2$]/F[DEZ]	F[DEZ] (mL·min^{-1})	F[$Mg(CpEt)_2$] (mL·min^{-1})	thickness after 200 cycles (nm)	growth rate (nm·s^{-1})
0	25	0	190	1.1
10	20	200	210	
20	10	200	130	
25	8	200	130	
33	6	200	131	0.54
45	4	180	70	0.46
60	4	240	100	
75	6.7	500	125	
88	5.7	500	100	0.51
125	4	500	55	
300	1.67	500	21	
625	0.80	500	17	

[a] $Mg(CpEt)_2$ is heated to 55 °C. The growth rates shown were calculated from the plots in Figure S3 of the Supporting Information.

Film Characterization. Absorption measurements were performed using an Agilent/HP 8453 UV−visible spectrometer. X-ray photoelectron spectroscopy (XPS) measurements were performed using an XR6 monochromated Al K_α X-ray source ($h\nu$ = 1486.6 eV) with a spot size of 900 μm to measure the Mg content of the metal oxide films. The samples were measured inside an ultrahigh-vacuum chamber (ESCALAB 250Xi). The films measured were 10 nm thick on highly conductive gold substrates. Photoluminescence measurements were performed using an ACCENT RPM 2000 system with a Nd:YAG laser with a wavelength of 266 nm with 4.5 mW power. All measurements were performed at room temperature under ambient conditions. X-ray diffraction was performed using CuK_α radiation (wavelength of 1.5406 Å) in a Bruker D8 theta/theta system. Wide scans were performed with a step size of 0.04° and dwell time of 2.5 s. Fine scans were performed with a step size of 0.01° and dwell time of 2.5 s. Atomic force microscopy (AFM) topography images were obtained using a Veeco dimension 3100 (in tapping mode) with a MikroMasch Si tip, and an Agilent 5500 scanning probe microscope with a Bruker Sb-doped Si tip with a resonant frequency of 319−378 kHz. The microscope with a Navitar video camera from the Agilent 5500 system was used to obtain optical microscopy images. Cross-sectional scanning electron microscopy (SEM) was performed by cleaving the samples and sputtering a few nanometers of Au/Pd onto the cleaved surface using an Emitech sputter coater. The coated surface was electrically grounded using carbon tape and the surface imaged using a LEO VP-1530 field emission scanning electron microscope at 3 kV.

Device Fabrication and Testing. Hybrid photovoltaic devices were fabricated using poly(3-hexylthiophene-2,5-diyl) (P3HT, from Rieke) as the active layer. $Zn_{1-x}Mg_xO$ was first deposited onto ITO, then P3HT was spin-cast on top at 2000 rpm from a solution with 30 mg·mL^{-1} P3HT in chlorobenzene (from Sigma-Aldrich) maintained at 60 °C in a process similar to that reported in ref 3. Polyimide tape was applied to the bottom of the device to prevent the contact pins from shunting the device and three silver contacts thermally evaporated on top using a shadow mask in a similar process to that reported in ref 15. The active area for each device was 0.15 cm^2.

Device characterization was performed under simulated AM 1.5 G illumination with a Newport Oriel class A solar simulator corrected for spectral mismatch. The light intensity was 100 mW·cm^{-2}. The devices

DOI: 10.1021/am5073589
ACS Appl. Mater. Interfaces 2015, 7, 10684−10694

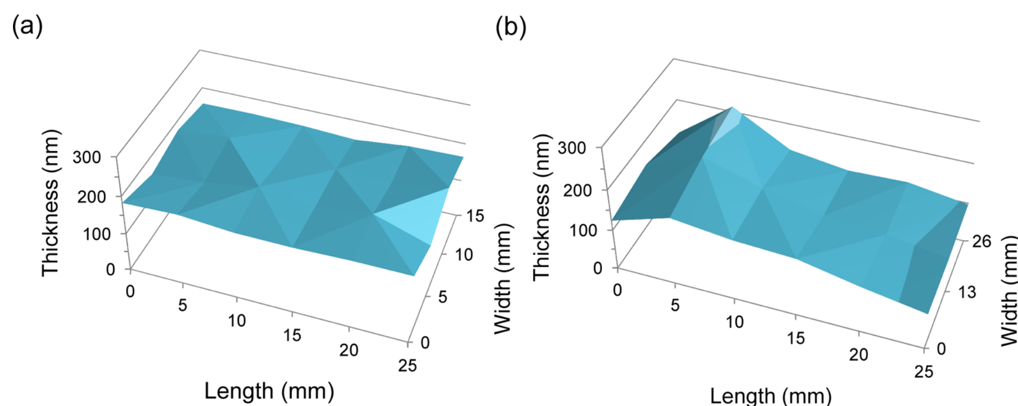

Figure 2. Thickness of AP-CVD ZnO films over a deposition area suitable for two small (14 mm by 14 mm or 12 mm by 12 mm)[3,15,21,26,30,34] square ITO/glass substrates for laboratory-scale electronic devices. Film profile for ZnO deposited using (a) our recently developed reactor compared to (b) our previous reactor detailed in ref 17, which had precursor gases flowing horizontally from left to right over the sample.

were masked to ensure the illuminated area was the same as the device area to prevent edge effects.

RESULTS AND DISCUSSION

An improvement in film thickness uniformity by changing the gas flow direction in our gas manifold is evident in Figure 2. For ZnO produced using our gas manifold, the film variation was only 3% of its thickness (Figure 2a), whereas the ZnO film produced with our previous design (which used horizontal gas flows) was more than twice as thick on the inlet side (left in Figure 2b) than on the exhaust side.

Our reactor design is similar to that reported by Ryan Fitzpatick et al.[36] A main difference is that instead of introducing the precursors via tubes within the gas channels in the manifold,[36] we introduced our precursor gases through both ends of channels running through the length of our manifold, from which the gases flowed vertically to the substrate (Figures 1b,c). Also, instead of pumping our exhaust gases, we used pressure gradients to drive the gases from their inlets to exhausts (Figure 1c). This leads to a simpler design and may play an important role in avoiding thickness variations due to unbalanced exhaust and inlet flows.[36]

Our manifold gas delivery design bears similarities to that used in some gas bearing reactors, e.g., the TNO reactor and head designed by the Eastman Kodak Company.[12,19] Combining a simple gas delivery design with a mechanically controllable substrate-manifold spacing allows us to achieve both uniform film deposition with the ability to deposit onto a variety of substrates, as discussed earlier.

The AP-CVD growth regime of our reaction can be seen from the $Zn_{1-x}Mg_xO$ film thickness linearly varying with metal precursor exposure time (Figure 3), with no evidence of growth rate saturation.[18] The exception could be $Zn_{0.8}Mg_{0.2}O$, which may have been deposited with a component of ALD growth (i.e., some chemisorption). AP-CVD growth occurred because (i) we used a large substrate-manifold spacing of 50 μm (compared to ~20 μm typically used in AP-SALD),[14,32,37] and (ii) we had different flow rates for the metal precursor channel (125−606.7 mL·min^{-1}) than in the oxidant (150 mL·min^{-1}) and inert (125 mL·min^{-1}) gas channels under the gas manifold.

The key advantage of growing films by AP-CVD rather than AP-SALD is that higher growth rates are achieved while retaining film crystallinity and compactness. For example, our ZnO growth rate of 1.1 nm·s^{-1} (Table 1) is higher than the growth rate of 0.63 nm·s^{-1} reported for our previous AP-SALD

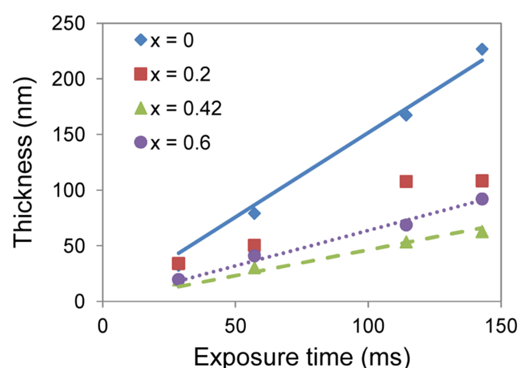

Figure 3. Plot of thickness vs exposure time of the substrate under the metal precursor channel in our deposition system to show the growth conditions. The compositions we display here and in subsequent figures are taken to be the same as those of the films specifically measured by XPS (details are in the Experimental Section).

gas manifold,[13] as well as being 2 orders of magnitude higher than that for conventional ALD,[12,14] and is comparable with some other AP-CVD reactors.[6] We produced crystalline films atmospherically at low temperatures of 150 °C (Figure 5 below and Figure S4 in the Supporting Information), which in CVD can typically only be achieved through plasma enhancement or at low pressures.[6,38,39] This suggests that the growth rate of our films was kinetically controlled by surface reactions and that the decomposition of the highly reactive precursors did not dominate the deposition process.[40] The dominance of surface rather than gas phase reactions could be aided by our substrate-manifold spacing (50 μm) being smaller than that used in CVD reactors (>1 cm), leading to less mixing of the precursors in the gas phase.[19,41−43] In addition, the N_2 gas channels in our reactor (Figure 1b,c) would further reduce the amount of precursor mixing in the gas phase. The morphology of our AP-CVD ZnO was also very similar to that of ALD ZnO (Figure S4a in the Supporting Information). Our AP-CVD reactor is additionally advantageous because the thickness of our films was linearly controlled by the number of cycles (Figure S3 in the Supporting Information). Thus, our AP-CVD reactor combines vertical gas flows using a simple design with a mechanically controlled substrate-manifold spacing. This combination gives the important advantages of film uniformity, compatibility with a wide variety of substrate types, high growth

DOI: 10.1021/am5073589
ACS Appl. Mater. Interfaces 2015, 7, 10684−10694

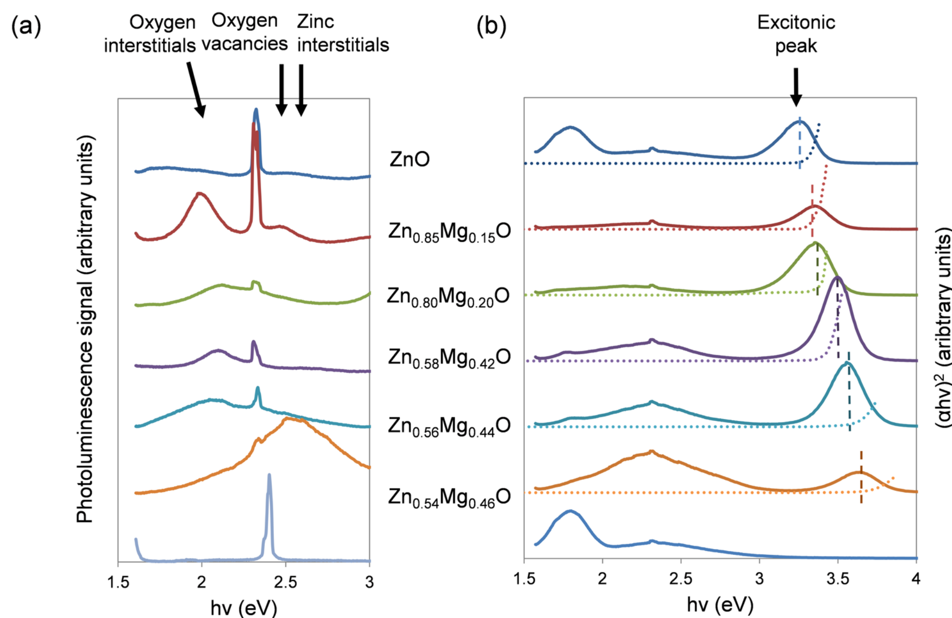

Figure 4. Photoluminescence measurements (solid lines) and Tauc plots (dashed lines) of $Zn_{1-x}Mg_xO$ films on (a) metallic copper and (b) ITO/glass with dashed lines to indicate the bandgap of the films. The bottom blue spectra are photoluminescence measurements of the blank substrates.

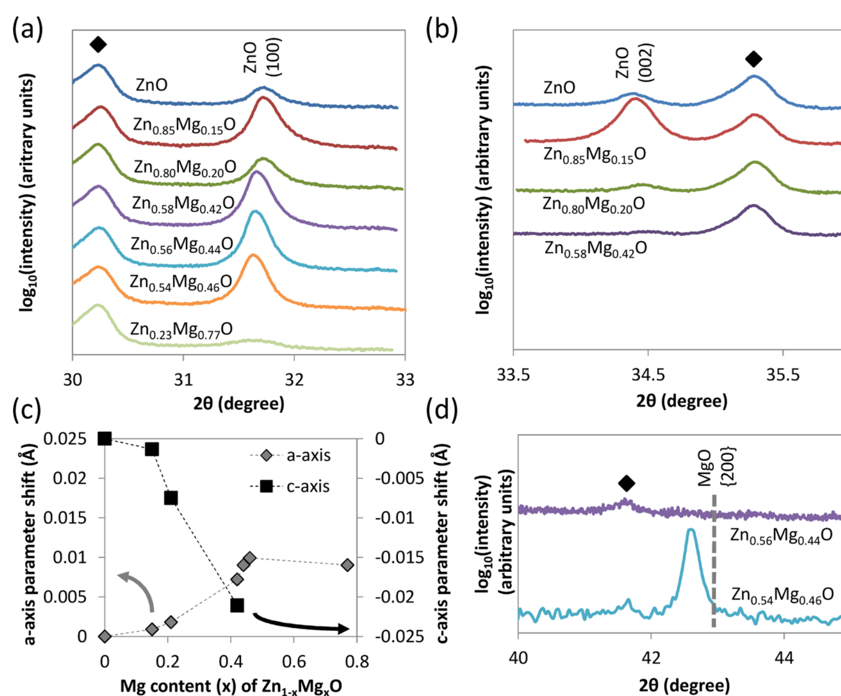

Figure 5. X-ray diffraction patterns of 200 nm thick $Zn_{1-x}Mg_xO$ deposited on ITO showing the shift in (a) the ZnO (100) peak and (b) the ZnO (002) peak with Mg incorporation (the step size was 0.01°, and dwell time was 2.5 s). The black diamonds indicate ITO peaks. (c) Shift in the *a*-axis and *c*-axis parameters of the wurtzite phase with Mg incorporation. (d) Comparison of the X-ray diffraction patterns of films with 44 at. % Mg and 46 at. % Mg showing that the film with 44 at. % Mg did not have a second rocksalt phase.

rates, crystallinity at deposition temperatures not exceeding 150 °C, and film thickness control.

To determine whether our reactor can control the incorporation of dopants into the metal oxide lattices to produce complex oxides, we analyzed Mg incorporation in ZnO using photoluminescence and X-ray diffraction (XRD) measurements. For photoluminescence measurements, the films were deposited onto copper foil because this was found to give a featureless photoluminescence background (with the exception of the laser harmonic at 2.33 eV), as can be seen in Figure 4a. From $x = 0$ to $x = 0.15$, defect peaks centered at 2 and 2.5 eV appeared, corresponding to oxygen interstitials and singly ionized oxygen vacancies, respectively.[44,45] For $x = 0.2$ to $x = 0.44$, the broad defect band was centered at 2.1 eV, which has been reported to correspond to oxygen interstitials, hydroxyl groups, and Li impurities.[44] While it is unlikely that Li impurities were present, hydroxyl groups could have been introduced due to the water oxidant used during film synthesis.

DOI: 10.1021/am5073589
ACS Appl. Mater. Interfaces 2015, 7, 10684−10694

Oxygen interstitials are the most likely cause of those defect peaks and are in agreement with the defect peaks found for x = 0.15. Oxygen vacancy peaks may also be present but obscured by the broadening from the oxygen interstitial peak.

These results indicate that the Mg^{2+} is incorporated substitutionally into the wurtzite ZnO lattice. The Mg^{2+} cation is slightly smaller than the Zn^{2+} cation[46,47] and, when occupying Zn^{2+} sites, would induce localized compressive strain, which may displace oxygen anions, leading to the creation of oxygen interstitials and oxygen vacancies.[48] Substitutional Mg incorporation to the lattice is consistent with the increase in bandgap shown from the blue-shift in the photoluminescence excitonic peak in Figure 4b, which is also in agreement with absorption measurements (Figure 4b and Figure S5 in the Supporting Information). In Figure 4, some of the Tauc plots measured by absorption are also shown in Figure S5 of the Supporting Information. Because of scaling, Figure S5 in the Supporting Information shows sub-bandgap absorption more obviously, as well as showing the absorption of films with higher Mg contents than that displayed in Figure 4. There are small differences between the bandgaps predicted by the Tauc plots and photoluminescence measurements in Figure 4b for some of the films because the measurements were obtained from different films. The photoluminescence measurements were obtained from films on ITO/glass (which are more relevant to our focus on device applications), whereas the Tauc plots were measured for films prepared on glass (since ITO also absorbs).

X-ray diffraction studies of the $Zn_{1-x}Mg_xO$ films on ITO confirmed that Mg^{2+} was substituting into the ZnO lattice. In Figure 5a, it can be seen that with Mg incorporation, the wurtzite (100) peak shifts to lower diffraction angles, whereas the wurtzite (002) peak shifts toward higher diffraction angles (Figure 5b). These correspond to the a-axis parameter increasing and c-axis parameter decreasing with Mg incorporation (Figure 5c), which is consistent with reports in the literature and indicates that the Mg^{2+} is indeed substituting into Zn^{2+} sites and distorting the lattice.[46,47,49,50] Also, the a-axis parameter of intrinsic ZnO was found to be 3.26 Å and the c-axis parameter to be 5.21 Å, which are both within the range reported in the literature for ZnO.[46,47,50,51]

For x = 0.46, there is a broad defect photoluminescence peak centered at 2.6 eV (Figure 4a), which is close to peaks that have been reported to correspond to oxygen vacancies (2.5 eV) and zinc interstitials (2.7 eV).[44,45] XRD measurements in Figure 6 indicate that the rocksalt MgZnO phase appears at this composition and coexists with the wurtzite $Zn_{1-x}Mg_xO$ phase. Since the total amount of oxygen in the lattice is unchanged, Mg separating to form the rocksalt phase would lead to less oxygen being available for the wurtzite lattice, leading to oxygen vacancies in the wurtzite phase. The rocksalt MgZnO phase is insulating, and thus, only the films solely containing wurtzite are useful for electronic applications. This onset of phase separation (46 at. % Mg) is much higher than the thermodynamic solubility limit of Mg in ZnO (4 wt %)[52] but is within the range of compositions (35 at. % to 68 at. %) reported for the appearance of a second phase in $Zn_{1-x}Mg_xO$ synthesized by other low-temperature techniques, in which it is reported that zinc magnesium oxide often forms a metastable phase.[53−56] A fine scan (with a step size of 0.01° as opposed to 0.04°) was employed to remeasure $Zn_{0.56}Mg_{0.44}O$, and no MgO{200} peak was found (Figure 5d). Although traces of an MgO {200} peak may be detected under a longer scan of 14 h,[57] the film mobilities[30] and current densities from our devices

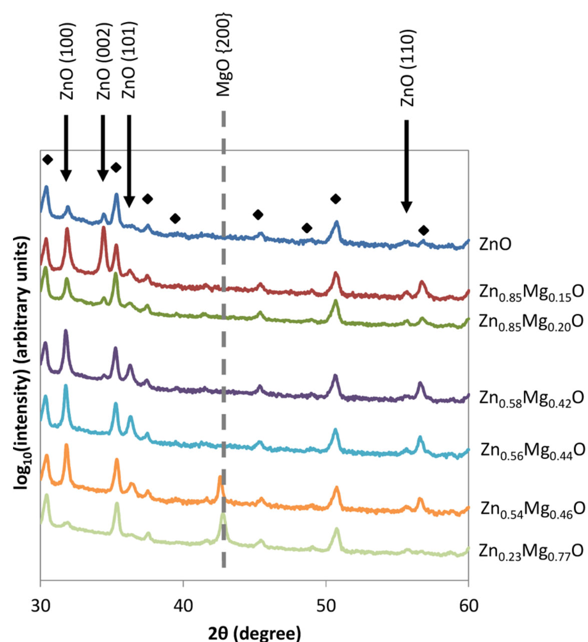

Figure 6. X-ray diffraction (XRD) measurements of 200 nm thick $Zn_{1-x}Mg_xO$ on ITO/glass. The trends are similar to those of the films on glass that we previously reported.[30] It is, however, important to analyze the XRD patterns of films on ITO/glass, which are used in electronic devices. Black diamonds indicate peaks corresponding to the ITO substrate. The diffraction peaks for ZnO and MgO are indicated.

(Figure S8, Supporting Information) did not significantly decrease until $x > 0.42$, indicating that the amount of rocksalt phase is negligible for $x \leq 0.42$. That no significant traces of a rocksalt phase was detected below the 46 at. % Mg threshold and the increasing rate of change in the lattice parameters with increasing Mg content up to that threshold (Figure 5c) indicate that there was no preferential incorporation of Mg into certain grains compared with others and hence that Mg was incorporated uniformly.[57]

Furthermore, when the films were annealed at 400 °C for 1 h in air and remeasured, the wurtzite-only films still did not exhibit any detectable phase separation (Figures S6 and S7d in the Supporting Information) and still showed a shift in the lattice parameters with Mg incorporation, indicating that the Mg^{2+} remained in the lattice (Figure S7 in the Supporting Information). This suggests that annealing at 400 °C (which is typically the highest postannealing temperature one would employ for ZnO films used in solar cells)[58] for 1 h is insufficient to induce significant macroscopic phase separation in the metastable $Zn_{1-x}Mg_xO$. Thus, photoluminescence and X-ray diffraction analyses show our reactor successfully allows Mg to be incorporated into the ZnO lattice, maintaining a stable single phase for contents below 46 at. % Mg.

The vapor pressure, reactivity, and saturation of the precursors are also important properties to understand when growing multicomponent films by chemical vapor deposition. Unlike photoluminescence measurements and X-ray diffraction patterns, it is more difficult to measure these properties because they require difficult techniques,[59] specific instruments, or the need to be measured dynamically in the system itself. However, we show that it is possible to gain an indication of these parameters to improve growth conditions by modeling the relationship between Mg content and bubbling rate ratio. We do not distinguish between different manifold designs in this

DOI: 10.1021/am5073589
ACS Appl. Mater. Interfaces 2015, 7, 10684−10694

model. It is assumed that film formation involves the metal precursor directly depositing onto the substrate, which can occur from activated species formed in the gas phase (chemical vapor deposition)[6] or chemisorption (atomic layer deposition).[9] Thus, although we only verify our model in this work for $Zn_{1-x}Mg_xO$ synthesized by our AP-CVD reactor, the model should be applicable to other systems. The relationship between the gas fraction of the Mg precursor fed to the gas manifold and molar flow rates to each of the metal precursor bubblers is given by eq 1.

$$\text{(gas fraction of Mg(CpEt)}_2\text{)} = \frac{\text{molar flow rate of Mg(CpEt)}_2}{\text{molar flow rate of Mg(CpEt)}_2 + \text{molar flow rate of DEZ}} \quad (1)$$

To predict the fraction of Mg in the film, the deposition rate of the Mg precursor (k_{Mg}) and Zn precursor (k_{Zn}) are needed. The saturation of both precursors (s_{Mg} and s_{Zn} respectively) to the flowing N_2 gas at the outlet of each bubbler is also needed, as well as the vapor pressure of the precursors. The full list of assumptions used and derivation of the model is given in section S2 of the Supporting Information. The final model is given by eq 2.

$$x = \frac{1}{1 + \frac{s_{Zn}}{s_{Mg}}\frac{k_{Zn}}{k_{Mg}}\frac{F[\text{DEZ}]}{F[\text{Mg(CpEt)}_2]}\cdot\frac{p^*_{Zn}(T_{Zn})}{p^*_{Mg}(T_{Mg})}} \quad (2)$$

In eq 2, x is the fraction of Mg in the film, $F[\text{DEZ}]$ the bubbling rate through the Zn precursor, $p^*_{Zn}(T_{Zn})$ the vapor pressure of the Zn precursor, $F[\text{Mg(CpEt)}_2]$ the bubbling rate through the Mg precursor, and $p^*_{Mg}(T_{Mg})$ the vapor pressure of the Mg precursor. The other parameters have been defined above. The independent variable is the ratio of the bubbling rates through the precursors ($F[\text{Mg(CpEt)}_2]/F[\text{DEZ}]$), and x is the parameter modeled. DEZ is well-studied, with several publications detailing its vapor pressure curve with a low level of discrepancy between them.[60−62] We therefore used the literature value of the DEZ vapor pressure (12.2 mmHg at 20 °C, as reported by Sigma-Aldrich, our supplier).[62] The saturation and deposition rates of the precursors and the vapor pressure of Mg(CpEt)_2 ($p^*_{Mg}(T_{Mg})$) are not as well known. We therefore introduced the parameter, β, where $\beta = s_{Zn}k_{Zn}/s_{Mg}k_{Mg}p^*_{Mg}(T_{Mg})$. Substituting this into eq 2 gave eq 3.

$$x = \frac{1}{1 + \beta\frac{F[\text{DEZ}]}{F[(\text{MgCpEt})_2]}p^*_{\text{Zn}}(T_{\text{Zn}})} \quad (3)$$

By rearranging eq 3, we can obtain a form (eq 4) allowing us to fit β to the experimental data (Figures 7b,c).

$$\frac{1}{x} = 1 + \beta p^*_{\text{Zn}}(T_{\text{Zn}})\frac{F[\text{DEZ}]}{F[\text{Mg(MgCpEt)}_2]} \quad (4)$$

Although the data could be fitted with one value of β (i.e., one linear region) in Figure 7b, such that the refined model (eq 4) fits the XPS measured Mg contents (Figure 7a) with a root-mean-square error of $\Delta x = 0.09$, it can be seen from Figure 7c that there are two distinct regions with two different values of β. This piecewise model has a root-mean-square deviation of $\Delta x = 0.0005$ from the experimental data (Figure 7a), showing that using two β values provides a very good fit of the data. The transition between the two regions occurs at $x = 0.42$, which is close to the point where the second rocksalt-based phase appears and coexists with wurtzite $Zn_{1-x}Mg_xO$ (Figure 6).[30] To further investigate this, we compared values of β^{-1} in the two regions since this is proportional to k_{Mg}/k_{Zn}, s_{Mg}/s_{Zn}, and the vapor pressure of Mg(CpEt)_2 (estimated from eq S20 of the Supporting Information to be 0.09 mmHg at 55 °C). It can be seen from Table 2 that in region 1 (wurtzite-only $Zn_{1-x}Mg_xO$), β^{-1} was lower than that in region 2, which indicates that the incorporation of Mg was higher in region 2.

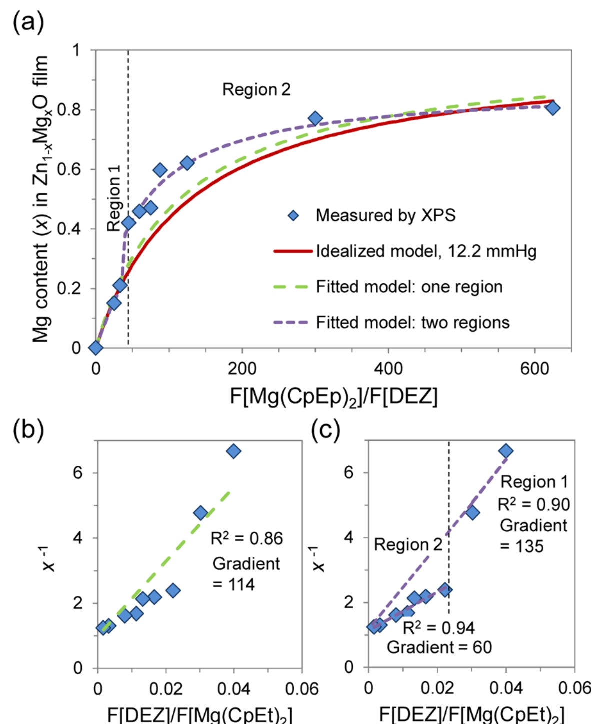

Figure 7. Model analysis for Mg(CpEt)_2 heated to 55 °C. (a) Plot of Mg content (x) in $Zn_{1-x}Mg_xO$ measured by X-ray photoelectron spectroscopy (XPS) vs the bubbling rate ratio between the Mg precursor and Zn precursor ($F[\text{Mg(CpEt)}_2]/F[\text{DEZ}]$). XPS provides accurate quantitative composition measurements.[63] The x values predicted by the idealized model (please refer to Section S2 of the Supporting Information) are shown (vapor pressure of Mg(CpEt)_2 at 55 °C used). The x values predicted by the models fitted to all the data (i.e., "one region") and fitted using a piecewise function (i.e., "two regions") are also shown. Fitting of x^{-1} vs the bubbling rate ratio through the Zn to Mg precursors ($F[\text{DEZ}]/F[\text{Mg(CpEt)}_2]$) with (b) one linear region and (c) two linear regions.

Table 2. Analysis of the Fitted Coefficient, β, from the Two-Region Fitted Model in Figure 7c

region	gradient	β value (mmHg^{-1})	β^{-1} (mmHg)
1	135	11.1	0.09
2	60	4.9	0.20

Our model indicates that an increase in the Mg incorporation for each bubbling rate ratio could be obtained by using the maximum bubbling rate through the Mg precursor (500 mLmin^{-1} in our setup). This can be seen in Figure 8b,c, in which a ~0.1 eV increase in the bandgap was obtained by bubbling at 500 mL·min^{-1} through the Mg precursor instead of 200 mL·min^{-1}, while keeping the bubbling rate ratio the same. This model therefore can assist in improving growth conditions without having to directly measure deposition rate or

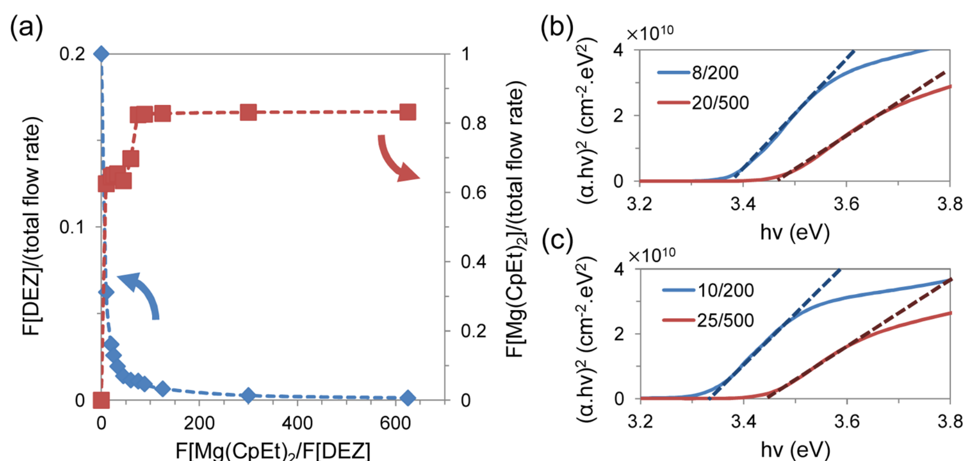

Figure 8. (a) Plot of the ratio of the bubbling rate through each precursor relative to the total flow rate through the metal gas line (F[DEZ] + F[Mg(CpEt)$_2$] + 100 mL·min^{-1}). Comparison of the bandgap of $Zn_{1-x}Mg_xO$ films synthesized by using bubbling rates of (b) 8/200 vs 20/500 and (c) 10/200 vs 25/500 (F[DEZ]/F[Mg(CpEt)$_2$]).

saturation. Since these require careful measurements, such as quartz crystal microgravimetry,[64] this is advantageous.

The increase in β^{-1} from regions 1 to 2 could be due to an increase in the incorporation rate of the Mg precursor relative to the Zn precursor. This may have resulted from an increased partial pressure of the Mg precursor relative to the Zn precursor. There are several ways in which this could have occurred. In Figure 8a, it can be seen that the bubbling rate through Mg(CpEt)$_2$ relative to the total flow rate in the metal precursor gas stream abruptly increased from 180 mL·min^{-1} to 500 mL·min^{-1} at a bubbling rate ratio of 45 (x = 0.42) and therefore corresponds to the transition from regions 1 to 2. The high bubbling rate would increase the partial pressure of the Mg precursor relative to that of the Zn precursor, which is continuously being more diluted in the metal precursor gas stream with increasing bubbling rate ratios (Figure 8a). The higher relative partial pressure of the Mg precursor would increase its relative deposition rate. Further increases in the Mg(CpEt)$_2$ concentration may arise from an increase in s_{Mg}/s_{Zn}. The higher bubbling rate of 500 mL·min^{-1} in region 2 increases the turbulence in the Mg precursor bubbler. This may have produced droplets carried by the rapid gas stream (complete atomization to produce an aerosol is unlikely)[65] or increased mass transfer to the N_2 through an increased interfacial area.[66]

We also note that since we did not constrain the vapor pressure or reactivity of the Mg precursor in eq 4, the change in temperature as this vapor, heated to 55 °C, was mixed with room temperature inert gas in unheated pipes (see Figure 1 for details) did not influence the applicability of our model.

To demonstrate the good functionality of the films produced using our reactor, we used the $Zn_{1-x}Mg_xO$ deposited in this work in hybrid solar cells with poly(3-hexylthiophene-2,5-diyl) (P3HT) (Figure 9). Previously, we found that high open-circuit voltages can be obtained in colloidal quantum dot and cuprous oxide solar cells by tuning the magnesium content in $Zn_{1-x}Mg_xO$.[21,30] Using our hybrid devices (structure in Figure 9a), we here show that this can be generally obtained in thin film solar cells and highlight the importance of producing multicomponent metal oxides by AP-CVD. For the films that were only 45 nm thick, Mg-incorporation led to the V_{OC} of the devices increasing from 0.35 V (x = 0) to 0.81 V (x = 0.77) (Figure 9b), leading to efficiency increases (Figure S8a, Supporting Information). The V_{OC} increase was partly due to

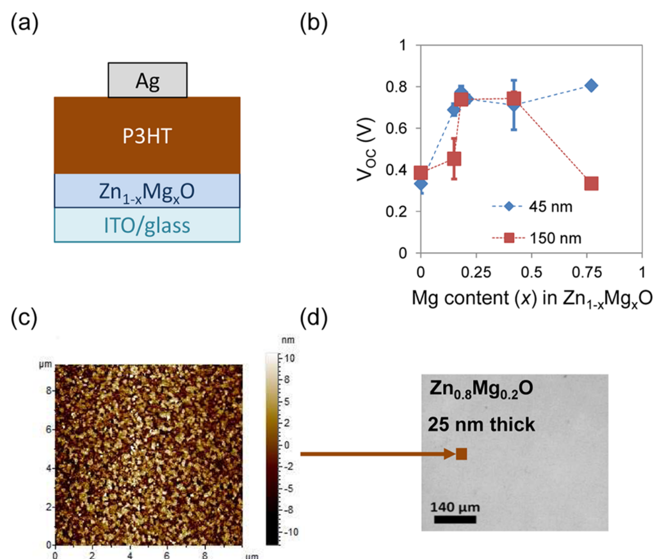

Figure 9. (a) Structure of the $Zn_{1-x}Mg_xO$ − (600 nm) P3HT hybrid device. (b) Change in the open-circuit voltage (V_{OC}) of $Zn_{1-x}Mg_xO$ − P3HT devices with Mg incorporation (x) for 45 and 150 nm thick $Zn_{1-x}Mg_xO$ films deposited at 150 °C. (c) AFM topography scan and (d) optical microscopy image of 25 nm thick $Zn_{0.8}Mg_{0.2}O$ film on ITO. The compositions we show are taken to be the same as those of the films specifically measured by XPS.

the built-in potential of the hybrid devices increasing as the conduction band of the $Zn_{1-x}Mg_xO$ was raised, which also reduces interfacial back-recombination.[4,67] Depositing 45 nm $Zn_{1-x}Mg_xO$ takes under 2 min over a 4 cm^2 area, and these films are thinner than those used in our previous work with quantum dot solar cells.[30] That such a large increase in V_{OC} could be obtained with films which are so thin indicates that the films are compact and pinhole-free since pinholes would have led to shunting.[15,68] The AFM image in Figure 9c of 25 nm $Zn_{1-x}Mg_xO$ on ITO confirms this, and the optical microscopy image in Figure 9d shows that no pinholes could be observed on a larger scale. The ability to produce high-performing films with a low thickness is advantageous due to a lower deposition time being required and because thinner films reduce the negative effect on device performance caused by the increasing resistivity of the films with Mg incorporation. This can be seen

DOI: 10.1021/am5073589
ACS Appl. Mater. Interfaces 2015, 7, 10684−10694

by comparing the devices with 45 nm versus 150 nm thick $Zn_{0.23}Mg_{0.77}O$ in Figure 9b. Because of the introduction of defect states (Figure 4) and increase in the effective electron mass,[69] the carrier concentration and mobility of $Zn_{1-x}Mg_xO$ films decrease with doping,[30] leading to a reduction in J_{SC}s (Figure S8b, Supporting Information). Being able to use thinner films allows electrons to be collected by the cathode before recombining, allowing higher V_{OC}s and J_{SC}s to be obtained.

CONCLUSIONS

In conclusion, we have detailed a gas manifold that is ideal for rapidly synthesizing high-quality multicomponent metal oxides with high functionality for electronics, as demonstrated for $Zn_{1-x}Mg_xO$. Our reactor has a manifold−substrate spacing that can be mechanically controlled independently of the precursor flow rates, and introduces the metal precursors vertically to the substrate with a uniform pressure profile across its length. These allow the films to be deposited onto a variety of substrate types with a set of properties highly suitable for electronics: high uniformity (3% thickness variation), high growth rate (up to 1.1 $nm \cdot s^{-1}$ for ZnO), crystalline films at low deposition temperatures (150 °C), and fine thickness control. The films are also highly compact, enabling the open-circuit voltage of hybrid P3HT solar cells to be more than doubled when using films only 45 nm thick. Photoluminescence and X-ray diffraction measurements also indicate that using this reactor enabled Mg to be incorporated into the ZnO lattice below 46 at. % Mg. We also developed a model that, through fitting the composition vs bubbling rate ratio, showed us that increased Mg incorporation can be achieved by increasing the bubbling rate through the Mg precursor. The laboratory-scale reactor we have developed is suitable for the production of high-quality oxides at a high rate for electronic applications.

ASSOCIATED CONTENT

Supporting Information

Detailed calculations, growth optimization procedure, supporting film characterization, and device performance measurements. The Supporting Information is available free of charge on the ACS Publications website at DOI: 10.1021/am5073589.

AUTHOR INFORMATION

Corresponding Author

*E-mail: jld35@cam.ac.uk.

Present Address

‖(Y.V.) Centre for Advanced Materials, Heidelberg University, Im Neuenheimer Feld 227, Heidelberg, Germany.

Notes

The authors declare no competing financial interest.

ACKNOWLEDGMENTS

We thank Dr. Giorgio Ercolano for useful discussions and technical assistance. We also acknowledge financial support from the Cambridge Commonwealth, European and International Trusts, Rutherford Foundation of New Zealand, the Marie Curie program (FP7/2007-2013, grant agreement numbers 219332 and 631111), the Comissionat per a Universitats I Recerca (CUR) del DIUE de la Generalitat de Catalunya (Spain), Girton College (Cambridge), and the ERC Advanced Investigator Grant, Novox, ERC-2009-adG 247276.

REFERENCES

(1) Musselman, K. P.; Schmidt-Mende, L. Nanostructured Inorganic Solar Cells. *Green* **2011**, *1*, 7−27.

(2) Kabra, D.; Lu, L. P.; Song, M. H.; Snaith, H. J.; Friend, R. H. Efficient Single-Layer Polymer Light-Emitting Diodes. *Adv. Mater.* **2010**, *22*, 3194−3198.

(3) Musselman, K. P.; Albert-Seifried, S.; Hoye, R. L. Z.; Sadhanala, A.; Muñoz-Rojas, D.; MacManus-Driscoll, J. L.; Friend, R. H. Improved Exciton Dissociation at Semiconducting Polymer:ZnO Donor:Acceptor Interfaces via Nitrogen Doping of ZnO. *Adv. Funct. Mater.* **2014**, *24*, 3562−3570.

(4) Hoye, R. L. Z.; Musselman, K. P.; MacManus-Driscoll, J. L. Doping ZnO and TiO_2 for Solar Cells. *APL Mater.* **2013**, *1*, 060701.

(5) Munk, B. H.; Schlegel, H. B. Molecular Orbital Studies of Zinc Oxide Chemical Vapor Deposition: Gas-Phase Radical Reactions. *Chem. Mater.* **2006**, *18*, 1878−1884.

(6) Illiberi, A.; Poodt, P.; Bolt, P.-J.; Roozeboom, F. Recent Advances in Atmospheric Vapor-Phase Deposition of Transparent and Conductive Zinc Oxide. *Chem. Vap. Deposition* **2014**, *20*, 234−242.

(7) Barnes, T. M.; Leaf, J.; Fry, C.; Wolden, C. A. Room Temperature Chemical Vapor Deposition of c-Axis ZnO. *J. Cryst. Growth* **2005**, *274*, 412−417.

(8) Kim, D.; Yun, I.; Kim, H. Fabrication of Rough Al Doped ZnO Films Deposited by Low Pressure Chemical Vapor Deposition for High Efficiency Thin Film Solar Cells. *Curr. Appl. Phys.* **2010**, *10*, S459−S462.

(9) George, S. M. Atomic Layer Deposition: An Overview. *Chem. Rev.* **2010**, *110*, 111−131.

(10) Torndahl, T.; Platzer-Bjorkman, C.; Kessler, J.; Edoff, M. Atomic Layer Deposition of $Zn_{1-x}Mg_xO$ Buffer Layers for Cu(In,Ga)-Se_2 Solar Cells. *Prog. Photovoltaics* **2007**, *15*, 225−235.

(11) Lee, Y. S.; Heo, J.; Siah, S. C.; Mailoa, J. P.; Brandt, R. E.; Kim, S. B.; Gordon, R. G.; Buonassisi, T. Ultrathin Amorphous Zinc-Tin-Oxide Buffer Layer for Enhancing Heterojunction Interface Quality in Metal-Oxide Solar Cells. *Energy Environ. Sci.* **2013**, *6*, 2112−2114.

(12) Illiberi, A.; Roozeboom, F.; Poodt, P. Spatial Atomic Layer Deposition of Zinc Oxide Thin Films. *ACS Appl. Mater. Interfaces* **2012**, *4*, 268−272.

(13) Muñoz-Rojas, D.; MacManus-Driscoll, J. Spatial Atmospheric Atomic Layer Deposition: A New Laboratory and Industrial Tool for Low-Cost Photovoltaics. *Mater. Horiz.* **2014**, *1*, 314.

(14) Hoye, R. L. Z.; Muñoz-Rojas, D.; Nelson, S. F.; Illiberi, A.; Poodt, P.; Roozeboom, F.; MacManus-Driscoll, J. L. Atmospheric Pressure Spatial Atomic Layer Deposition of ZnO Thin Films: Reactors, Doping, and Devices. *APL Mater.* **2015**, *3*, 040701.

(15) Hoye, R. L. Z.; Muñoz-Rojas, D.; Iza, D. C.; Musselman, K. P.; MacManus-Driscoll, J. L. High Performance Inverted Bulk Heterojunction Solar Cells by Incorporation of Dense, Thin ZnO Layer Made Using Atmospheric Atomic Layer Deposition. *Sol. Energy Mater. Sol. Cells* **2013**, *116*, 197−202.

(16) Muñoz-Rojas, D.; Jordan, M.; Yeoh, C.; Marin, A. T.; Kursumovic, A.; Dunlop, L. A.; Iza, D. C.; Chen, A.; Wang, H.; MacManus-Driscoll, J. L. Growth of 5 $cm^2V^{-1}s^{-1}$ Mobility, P-Type Copper(I) Oxide (Cu_2O) Films by Fast Atmospheric Atomic Layer Deposition (AALD) at 225°C and Below. *AIP Adv.* **2012**, *2*, 042179.

(17) Muñoz-Rojas, D.; Sun, H.; Iza, D. C.; Weickert, J.; Chen, L.; Wang, H.; Schmidt-Mende, L.; MacManus-Driscoll, J. L. High-Speed Atmospheric Atomic Layer Deposition of Ultra Thin Amorphous TiO_2 Blocking Layers at 100 °C for Inverted Bulk Heterojunction Solar Cells. *Prog. Photovoltaics* **2013**, *21*, 393−400.

(18) Levy, D. H.; Freeman, D.; Nelson, S. F.; Cowdery-Corvan, P. J.; Irving, L. M. Stable ZnO Thin Film Transistors by Fast Open Air Atomic Layer Deposition. *Appl. Phys. Lett.* **2008**, *92*, 192101.

(19) Levy, D. H.; Nelson, S. F.; Freeman, D. Oxide Electronics by Spatial Atomic Layer Deposition. *J. Dispersion Technol.* **2009**, *5*, 484−494.

(20) Fotiadis, D. I.; Kremer, A. M.; McKenna, D. R.; Jensen, K. F. Complex Flow Phenomena in Vertical MOCVD Reactors: Effects on

Deposition Uniformity and Interface Abruptness. *J. Cryst. Growth* **1987**, *85*, 154−164.
(21) Hoye, R. L. Z.; Heffernan, S.; Ievskaya, Y.; Sadhanala, A.; Flewitt, A. J.; Friend, R. H.; MacManus-Driscoll, J. L.; Musselman, K. P. Engineering Schottky Contacts in Open-Air Fabricated Heterojunction Solar Cells to Enable High Performance and Ohmic Charge Transport. *ACS Appl. Mater. Interfaces* **2014**, *6*, 22192−22198.
(22) Poodt, P.; Cameron, D. C.; Dickey, E.; George, S. M.; Kuznetsov, V.; Parsons, G. N.; Roozeboom, F.; Sundaram, G.; Vermeer, A. Spatial Atomic Layer Deposition: A Route towards Further Industrialization of Atomic Layer Deposition. *J. Vac. Sci. Technol. A* **2012**, *30*, 010802.
(23) Illiberi, A.; Simons, P. J. P. M.; Kniknie, B.; van Deelen, J.; Theelen, M.; Zeman, M.; Tijssen, M.; Zijlmans, W.; Steijvers, H. L. A. H.; Habets, D.; Janssen, A. C.; Beckers, E. H. A. Growth of ZnO_x:Al by High-Throughput CVD at Atmospheric Pressure. *J. Cryst. Growth* **2012**, *347*, 56−61.
(24) Illiberi, A.; Cobb, B.; Sharma, A.; Grehl, T.; Brongersma, H.; Roozeboom, F.; Gelinck, G.; Poodt, P. Spatial Atmospheric Atomic Layer Deposition of $In_xGa_yZn_zO$ for Thin Film Transistors. *ACS Appl. Mater. Interfaces* **2015**, *7*, 3671−3675.
(25) Ellinger, C. R.; Nelson, S. F. Selective Area Spatial Atomic Layer Deposition of ZnO, Al_2O_3, and Aluminum-Doped ZnO Using Poly(vinyl Pyrrolidone). *Chem. Mater.* **2014**, *26*, 1514−1522.
(26) Ievskaya, Y.; Hoye, R. L. Z.; Sadhanala, A.; Musselman, K. P.; MacManus-Driscoll, J. L. Fabrication of ZnO/Cu_2O Heterojunctions in Atmospheric Conditions: Improved Interface Quality and Solar Cell Performance. *Sol. Energy Mater. Sol. Cells* **2014**, *135*, 43−48.
(27) Wang, F.; Tan, Z.; Li, Y. Solution-Processable Metal Oxides/Chelates as Electrode Buffer Layers for Efficient and Stable Polymer Solar Cells. *Energy Environ. Sci.* **2015**, *8*, 1059−1091.
(28) Concina, I.; Vomiero, A. Metal Oxide Semiconductors for Dye- and Quantum-Dot-Sensitized Solar Cells. *Small* **2014**, *11*, 1744−1774.
(29) Iza, D. C.; Muñoz-Rojas, D.; Musselman, K. P.; Weickert, J.; Jakowetz, A. C.; Sun, H.; Ren, X.; Hoye, R. L. Z.; Lee, J. H.; Wang, H.; Schmidt-Mende, L.; MacManus-Driscoll, J. L. Nanostructured Conformal Hybrid Solar Cells: A Promising Architecture towards Complete Charge Collection and Light Absorption. *Nanoscale Res. Lett.* **2013**, *8*, 359.
(30) Hoye, R. L. Z.; Ehrler, B.; Böhm, M. L.; Muñoz-Rojas, D.; Altamimi, R. M.; Alyamani, A. Y.; Vaynzof, Y.; Sadhanala, A.; Ercolano, G.; Greenham, N. C.; Friend, R. H.; MacManus-Driscoll, J. L.; Musselman, K. Improved Open-Circuit Voltage in ZnO-PbSe Quantum Dot Solar Cells by Understanding and Reducing Losses Arising from the ZnO Conduction Band Tail. *Adv. Energy Mater.* **2014**, *4*, 1301544.
(31) Sinsermsuksakul, P.; Hartman, K.; Bok Kim, S.; Heo, J.; Sun, L.; Hejin Park, H.; Chakraborty, R.; Buonassisi, T.; Gordon, R. G. Enhancing the Efficiency of SnS Solar Cells via Band-Offset Engineering with a Zinc Oxysulfide Buffer Layer. *Appl. Phys. Lett.* **2013**, *102*, 053901.
(32) Illiberi, A.; Scherpenborg, R.; Wu, Y.; Roozeboom, F.; Poodt, P. Spatial Atmospheric Atomic Layer Deposition of $Al_xZn_{1-x}O$. *ACS Appl. Mater. Interfaces* **2013**, *5*, 13124−13128.
(33) Illiberi, A.; Scherpenborg, R.; Roozeboom, F.; Poodt, P. Atmospheric Spatial Atomic Layer Deposition of In-Doped ZnO. *ECS J. Solid State Sci. Technol.* **2014**, *3*, P111−P114.
(34) Hoye, R. L. Z.; Chua, M. R.; Musselman, K. P.; Li, G.; Lai, M.-L.; Tan, Z.-K.; Greenham, N. C.; MacManus-Driscoll, J. L.; Friend, R. H. Enhanced Performance in Fluorene-Free Organometal Halide Perovskite Light Emitting Diodes Using Tunable, Low Electron-Affinity Oxide Electron-Injectors. *Adv. Mater.* **2015**, *27*, 1414−1419.
(35) Hoye, R. L. Z.; Brandt, R. E.; Ievskaya, Y.; Heffernan, S.; Musselman, K. P.; Buonassisi, T.; MacManus-Driscoll, J. L. Perspective: Maintaining Surface-Phase Purity is Key to Efficient Open Air Fabricated Cuprous Oxide Solar Cells. *APL Mater.* **2015**, *3*, 020901.
(36) Ryan Fitzpatrick, P.; Gibbs, Z. M.; George, S. M. Evaluating Operating Conditions for Continuous Atmospheric Atomic Layer Deposition Using a Multiple Slit Gas Source Head. *J. Vac. Sci. Technol. A* **2012**, *30*, 01A136.
(37) Nelson, S. F.; Levy, D. H.; Tutt, L. W.; Burberry, M. Cycle Time Effects on Growth and Transistor Characteristics of Spatial Atomic Layer Deposition of Zinc Oxide. *J. Vac. Sci. Technol. A* **2012**, *30*, 01A154.
(38) Barnes, T. M.; Leaf, J.; Fry, C.; Wolden, C. A. Room Temperature Chemical Vapor Deposition of c-Axis ZnO. *J. Cryst. Growth* **2005**, *274*, 412−417.
(39) Nicolay, S.; Faÿ, S.; Ballif, C. Growth Model of MOCVD Polycrystalline ZnO. *Cryst. Growth Des.* **2009**, *9*, 4957−4962.
(40) Jones, A. C.; Hitchman, M. L. *Chemical Vapour Deposition: Precursors, Processes and Applications*, 1st ed.; The Royal Society of Chemistry: Cambridge, UK, 2009.
(41) Hu, J.; Gordon, R. G. Textured Aluminum-Doped Zinc Oxide Thin Films from Atmospheric Pressure Chemical-Vapor Deposition. *J. Appl. Phys.* **1992**, *71*, 880.
(42) Haga, K.; Katahira, F.; Watanabe, H. Preparation of ZnO Films by Atmospheric Pressure Chemical-Vapor Deposition Using Zinc Acetylacetonate and Ozone. *Thin Solid Films* **1999**, *343−344*, 145−147.
(43) Kumar, N. D.; Kamalasanan, M. N.; Chandra, S. Metalorganic Chemical Vapor Deposition Technique for Growing c-Axis Oriented ZnO Thin Films in Atmospheric Pressure Air. *Appl. Phys. Lett.* **1994**, *65*, 1373.
(44) Djurišić, A. B.; Ng, A. M. C.; Chen, X. Y. ZnO Nanostructures for Optoelectronics: Material Properties and Device Applications. *Prog. Quantum Electron.* **2010**, *34*, 191−259.
(45) Fujihara, S.; Ogawa, Y.; Kasai, A. Tunable Visible Photoluminescence from ZnO Thin Films through Mg-Doping and Annealing. *Chem. Mater.* **2004**, *16*, 2965−2968.
(46) Etacheri, V.; Roshan, R.; Kumar, V. Mg-Doped ZnO Nanoparticles for Efficient Sunlight-Driven Photocatalysis. *ACS Appl. Mater. Interfaces* **2012**, *4*, 2717−2725.
(47) Bai, L.-N.; Lian, J.-S.; Jiang, Q. Optical and Electronic Properties of Wurtzite Structure $Zn_{1-x}Mg_xO$ Alloys. *Chin. Phys. Lett.* **2011**, *28*, 117101.
(48) Chen, Q.; Braun, A.; Yoon, S.; Bagdassarov, N.; Graule, T. Effect of Lattice Volume and Compressive Strain on the Conductivity of BaCeY-Oxide Ceramic Proton Conductors. *J. Eur. Ceram. Soc.* **2011**, *31*, 2657−2661.
(49) Kumar, P.; Singh, J. P.; Kumar, Y.; Gaur, A.; Malik, H. K.; Asokan, K. Investigation of Phase Segregation in $Zn_{1-x}Mg_xO$ Systems. *Curr. Appl. Phys.* **2012**, *12*, 1166−1172.
(50) Zhang, X.; Li, X. M.; Chen, T. L.; Bian, J. M.; Zhang, C. Y. Structural and Optical Properties of $Zn_{1-x}Mg_xO$ Thin Films Deposited by Ultrasonic Spray Pyrolysis. *Thin Solid Films* **2005**, *492*, 248−252.
(51) Jagadish, C., Pearton, S. J., Eds. *Zinc Oxide Bulk, Thin Films and Nanostructures*, 1st ed.; Elsevier Ltd.: Oxford, UK, 2007.
(52) Segnit, E. R.; Holland, A. E. The System MgO-ZnO-SiO_2. *J. Am. Ceram. Soc.* **1965**, *48*, 409−413.
(53) Ellmer, K.; Klein, A.; Bernd, R., Eds. *Transparent Conductive Zinc Oxide: Basics and Applications in Solar Cells*, 1st ed.; Springer: Heidelberg, Germany, 2008.
(54) Schmidt-Grund, R.; Carstens, A.; Rheinländer, B.; Spemann, D.; Hochmut, H.; Zimmermann, G.; Lorenz, M.; Grundmann, M.; Herzinger, C. M.; Schubert, M. Refractive Indices and Band-Gap Properties of Rocksalt $Mg_xZn_{1-x}O$ ($0.68 \leq x \leq 1$). *J. Appl. Phys.* **2006**, *99*, 123701.
(55) Minemoto, T.; Negami, T.; Nishiwaki, S.; Takakura, H. Preparation of $Zn_{1-x}Mg_xO$ Films by Radio Frequency Magnetron Sputtering. *Thin Solid Films* **2000**, *372*, 173−176.
(56) Chen, J.; Shen, W. Z.; Chen, N. B.; Qiu, D. J.; Wu, H. Z. The Study of Composition Non-uniformity in Ternary $Mg_xZn_{1-x}O$ Thin Films. *J. Phys.: Condens. Matter* **2003**, *15*, L475−L482.
(57) Thapa, D.; Huso, J.; Che, H.; Huso, M.; Morrison, J. L.; Gutierrez, D.; Grant Norton, M.; Bergman, L. Probing Embedded Structural Inhomogeneities in MgZnO Alloys via Selective Resonant Raman Scattering. *Appl. Phys. Lett.* **2013**, *102*, 191902.

(58) Iza, D. C.; Muñoz-Rojas, D.; Jia, Q.; Swartzentruber, B.; Macmanus-Driscoll, J. L. Tuning of Defects in ZnO Nanorod Arrays Used in Bulk Heterojunction Solar Cells. *Nanoscale Res. Lett.* **2012**, *7*, 655.

(59) *Standard Test Method for Vapor Pressure-Temperature Relationship and Initial Decomposition Temperature of Liquids by Isoteniscope*; ASTM International: West Conshohocken, PA, 2010; ASTM D2879-10.

(60) Stull, D. R. Vapor Pressure of Pure Substances Organic Compounds. *Ind. Eng. Chem.* **1947**, *39*, 517−540.

(61) Kuniya, Y.; Deguchi, Y. Physicochemical Properties of Dimethylzinc, Dimethylcadmium and Diethylzinc. *Appl. Organomet. Chem.* **1991**, *5*, 337−347.

(62) Diethylzinc; SAFC Hitech. URL: http://www.sigmaaldrich.com/content/dam/sigma-aldrich/docs/Sigma-Aldrich/General_Information/epichem-zinc.pdf.

(63) Hüfner, S. *Photoelectron Spectroscopy: Principles and Applications*, 3rd ed.; Springer: Heidelberg, Germany, 2003.

(64) Yousfi, E. B.; Fouache, J.; Lincot, D. Study of Atomic Layer Epitaxy of Zinc Oxide by in-Situ Quartz Crystal Microgravimetry. *Appl. Surf. Sci.* **2000**, *153*, 223−234.

(65) Sovani, S.; Sojka, P.; Lefebvre, A. Effervescent Atomization. *Prog. Energy Combust. Sci.* **2001**, *27*, 483−521.

(66) Monteith, A. H. D.; Bell, J. P.; Parker, W. J.; Melcer, H.; Harvey, R. T.; Parker, J.; Monteith, H. D. Effect of Bubble-Induced Surface Turbulence on Gas-Liquid Mass Transfer in Diffused Aeration Ssytems. *Water Environ. Res.* **2015**, *77*, 128−137.

(67) Olson, D. C.; Shaheen, S. E.; White, M. S.; Mitchell, W. J.; van Hest, M. F. A. M.; Collins, R. T.; Ginley, D. S. Band-Offset Engineering for Enhanced Open-Circuit Voltage in Polymer−Oxide Hybrid Solar Cells. *Adv. Funct. Mater.* **2007**, *17*, 264−269.

(68) Musselman, K. P.; Marin, A.; Wisnet, A.; Scheu, C.; MacManus-Driscoll, J. L.; Schmidt-Mende, L. A Novel Buffering Technique for Aqueous Processing of Zinc Oxide Nanostructures and Interfaces, and Corresponding Improvement of Electrodeposited ZnO-Cu2O Photovoltaics. *Adv. Funct. Mater.* **2011**, *21*, 573−582.

(69) Cohen, D. J.; Ruthe, K. C.; Barnett, S. A. Transparent Conducting $Zn_{1-x}Mg_xO$:(Al,In) Thin Films. *J. Appl. Phys.* **2004**, *96*, 459.

DOI: 10.1021/am5073589
ACS Appl. Mater. Interfaces 2015, 7, 10684−10694